Journal of Solid State Chemistry **142,** 63–73 (1999)
Article ID jssc.1998.7986, available online at http://www.idealibrary.com on IDEAL®

The Scanning–Tunneling Microscopy, the X-Ray Photoelectron Spectroscopy, the Inner-Shell-Electron Energy-Loss Spectroscopy Studies of MTe$_2$ and M_3SiTe$_6$ (M = Nb and Ta)

Youichi Ohno

Department of Electrical and Electronic Engineering, Faculty of Engineering, Utsunomiya University, 2753 Ishii-machi, Utsunomiya 321, Tochigi, Japan

Recieved March 27, 1998; in revised form July 14, 1998; accepted July 24, 1998

The Ta $N_{6,7}$ and Te $N_{4,5}$ inner-shell-electron energy-loss spectroscopy (ISEELS) spectra and the X-ray photoelectron spectroscopy (XPS) spectra in layered transition-metal ditellurides MTe$_2$ (M = Ta, Nb) for which metal d-derived conduction bands overlap Te 5p valence bands significantly, have been measured to study the effects of band structure on the final states and the valences of constituent atoms. For comparison we have obtained the ISEELS and XPS spectra of M_3SiTe$_6$, which crystallizes in a layer structure akin to that of MTe$_2$. The atomically resolved scanning–tunneling microscopy (STM) images of NbTe$_2$ and Ta$_3$SiTe$_6$ have been obatined to investigate a surface atomic structure as well as a surface electronic structure. It is found that the Ta 4f and Te 4d XPS spectra in MTe$_2$ reveal a dominant peak for each spin orbit (s.o.) component although two-thirds of M atoms shift from undistorted octahedral sites to form double zigzag chains along the b axis and the STM images indicate the existence of three different kinds of Te sites. The Ta $N_{6,7}$ and Te $N_{4,5}$ ISEELS spectra reveal a doublet for each (s.o.) component. It arises from two different final states, that is, Ta^{3+*} 4f^{13}5d^2 and Ta^{4+*} 4f^{13}5d^1 for the Ta $N_{6,7}$ spectrum and Te^{2-*} 4$d^9$5p^6 and Te^{-*} 4$d^9$5p^5 for the Te $N_{4,5}$ spectrum. The final-state valence fluctuation model is proposed to explain the experimental result. © 1999 Academic Press

INTRODUCTION

Among various layered materials, the groups IV-, V-, and VI-a transition-metal dichalcogenides (TX_2) are extensively studied (1–3). They form a large family of compounds with quasi-two-dimensional physical and chemical properties such as charge density waves (CDW). They produce new exotic compounds with various anisotropic electrical, magnetic, and optical properties by intercalating foreign atoms, ions, and molecules into van der Waals gaps. The misfit-layer compounds $(MX)_x(TX_2)_m$ (M = Sn, Pb, Bi, Sb, and rare-earth metals; T = transition metals; $X = S$ and Se; $x = 0.08$–0.28; $m = 1$, 2, 3, and 4) and the multilayer compounds $A_y(MX)_x(TX_2)_2$ (A = alkali metals and Cu), which consist of one-atom-thick A layers, two-atom-thick MX layers, and three-atom-thick TX_2 layers regularly stacked in a direction normal to the layers, belong to the family of intercalation derivatives of layered transition-metal dichalcogenides (LTMD) in a broad sense. Recently, the crystal structure and the electronic structure has been studied extensively by many workers (4, 5). For transition-metal ditellurides, however, few studies have been made on electrical, magnetic, and optical properties. No misfit-layer compounds and no multilayer compounds have been synthesized from the tellurides, because their properties are considered to resemble those of the disulfides and the diselenides. However, metal atoms in the group V-a transition-metal ditellurides 1T-MTe$_2$ (M = V, Nb, and Ta) form double zigzag chains in a crystal and Te 5p-derived valence bands have empty states near the top region (6). The recent tight-binding band calculations of Canadell *et al.* (7) indicate that there is a stronger interaction between metal and Te atoms and among ligand atoms and that the Te 5p-derived valence bands overlap metal d bands significantly. A local chemical-bonding consideration suggests that the lattice distortion brings about a considerable electron transfer from the Te 5p valence bands to the metal d bands and that the formal d electron count is $d^{4/3}$ (8). These suggestions are confirmed by the recent tight-binding band calculations.

Ta$_3$SiTe$_6$ and Nb$_3$SiTe$_6$ are also layered tellurides, which contain two different types of metal and Te atoms in a crystal, that is, paired and isolated atoms (9, 10). Bengel and coworkers (11, 12) indicate that paired Te atoms appear as brighter spots than isolated Te atoms on the atomic force microscopy (AFM) images, whereas isolated Te atoms appear as brighter spots than paired Te atoms on the scanning tunneling microscopy (STM) images. The tight-binding band calculations of Boucher *et al.* (13) show that the compounds are metallic, having unoccupied states near the top of the valence bands. The unoccupied states contain a Nb 4d character. The next set of Nb 4d bands are separated from the valence bands by an energy gap.

This paper presents the scanning-tunneling microscopy (STM), the X-ray photoelectron spectroscopy (XPS), and

0022-4596/99 $30.00
Copyright © 1999 by Academic Press
All rights of reproduction in any form reserved.

the inner-shell-electron energy-loss spectroscopy studies of $1T$-$M\mathrm{Te}_2$ and $M_3\mathrm{SiTe}_6$ (M = Nb and Ta). The XPS and ISEELS spectra of $1T$-$M\mathrm{Te}_2$ give indirect evidences of strong metal–tellurium interaction. The Ta 4*f* and Te 4*d* XPS spectra show a dominant peak for each spin-orbit (s.o.) component, whereas the Ta $N_{6,7}$ and Te $N_{4,5}$ ISEELS spectra show a doublet arising from two different final states. We propose a final-state valence fluctuation model to interpret it. First, the STM images are discussed in relation to the crystal structure and the surface electronic structure. Next, the Ta $N_{6,7}$ and Te $N_{4,5}$ ISEELS spectra in $1T$-$M\mathrm{Te}_2$ are discussed together with the Nb $N_{2,3}$ ISEELS spectrum and the Ta 4*f* and Te 4*d* XPS spectra. For comparison, we have discussed the ISEELS and the XPS spectra of $1T$-TaS_2 in which a CDW lattice distortion is found at room temperature. Successively, the Ta $N_{6,7}$ and Te $N_{4,5}$ ISEELS spectra in $M_3\mathrm{SiTe}_6$ are discussed together with the Nb $N_{2,3}$ and Nb $M_{4,5}$ ISEELS spectra and the Ta 4*f* and Te 4*d* XPS spectra. Last, the final state effect and the band structure effect on the ISEELS and XPS spectra are discussd.

EXPERIMENTS

The single crystals of $1T$-TaS_2, $1T$-TaTe_2, $1T$-NbTe_2, $\mathrm{Ta}_3\mathrm{SiTe}_6$, and $\mathrm{Nb}_3\mathrm{SiTe}_6$ are grown from composite elements by chemical-vapor-transport reaction in a sealed silica ampoule. A small amount of iodine is added as a transport reagent. The crystals are analyzed by means of the X-ray powder diffraction method. Atomically clean and smooth surfaces are prepared by cleaving with adhesive tape in the atmosphere just before the measurements.

Our STM instrument is designed as an ultra-high vacuum (UHV) system to prevent a surface contamination. It is composed of an electronic control system, a tip driving system, a data acquisition and processing system with a personal computer, and a vacuum system which is divided into three parts; a sample exchange part with a turbo-molecular pump and an oil rotary pump, a surface preparation part with a combination pump, and a STM analysis part with an ion pump. A mechanically polished Pt–Ir tip is moved into a tunneling regime by means of coarse and fine mechanical drives and a piezoelectric drive. The STM measurements have been carried out at room temperature. The vacuum during the measurements is kept in the range of 10^{-8} to low 10^{-7} Pa. The images have been obtained in the constant current mode. During measurements, samples are kept at positive potential with respect to a tip. Atomically resolved images are obtained under the conditions that bias voltage is typically 0.1 V and tunneling current is about 1.0 nA.

Ta $N_{6,7}$, Te $N_{4,5}$, Nb $N_{2,3}$ and Nb $M_{4,5}$ ISEELS spectra have been measured at low incident energy in reflection geometry. A double-pass cylindrical-mirror analyzer (CMA) (PHI Model 15-255G), which is equipped with a coaxial normal-incidence electron gun, is employed. The measurements have been carried out at relatively large momentum transfer under ultra-high vacuum conditions of about 10^{-8} Pa. Momentum transfer, which is an important parameter in determining the transition-matrix elements of inelastic scattering, is given by

$$q = \frac{\sqrt{2m}}{\hbar}\{2E_o - \Delta E - 2E_o^{1/2}(E_o - \Delta E)^{1/2}\cos\theta_i\}^{1/2}, \quad [1]$$

where E_o is incident energy, ΔE is energy loss, and θ_i is an inelastic scattering angle. A large part of inelastic events occur at small inelastic-scattering angles. Then momentum transfer increases with decreasing incident energy. Hence, ISEELS spectra at low incident energy allow optically forbidden transitions due to breakdown of dipole selection rules, whereas at high incident energy they obey dipole selection rules like the X-ray absorption spectroscopy (XAS) spectra. The ISEELS spectra of shallow core-levels have a large background which arises from the emission of a great number of secondary electrons. To remove the background, the spectra are obtained in the second derivative form, using a lock-in amplifier.

Ta 4*f*, Te 4*d*, Nb 4*p*, and Nb 3*d* XPS spectra are measured in the pulse counting mode with unmonochromatized Mg$K\alpha$ radiations. A CMA analyzer, a UHV system, and data acquisition and processing systems are used commonly in XPS and ISEELS. A more detail description of our apparatus has been given in a previous paper (14).

RESULTS AND DISCUSSION

STM Results of $1T$-MTe_2 *and* M_3SiTe_6 (M = *Nb and Ta*)

The crystal structure of the group V-a transition-metal ditellurides is shown in Fig. 1. Double zigzag chains of metal atoms are formed along the b axis and the crystal lattice is distorted from a hexagonal to a monoclinic. The relationship of the two lattice constants is given by $a_m \approx 3\sqrt{3}a_h$, $b_m \approx a_h$, and $c_m \approx c_h \sin\beta$, where a_m, b_m, c_m, and β are parameters for monoclinic structure and a_h and c_h are parameters for undistorted hexagonal structure. The compounds are regarded as the distorted $1T$ type of LTMDs. Two-thirds of transition-metal atoms shift by about 0.5 Å from undistorted octahedral sites and the remaining one-third occupy nearly regular octahedral sites. The previous AFM studies of TaTe_2 and NbTe_2 made it clear that the top corrugated Te sheet was affected strongly by the modulation of a metal layer underneath it (15, 16). The AFM images show repeated triple rows of spots; two bright rows and one dim row represent higher- and lower-height atomic rows of Te, respectively. The results are confirmed by the present STM study. The STM images of NbTe_2 are shown in Figs. 2a and 2b. On the face of it Te atoms at the site A ($z = 0.3020$) are imaged more brightly than those at the sites

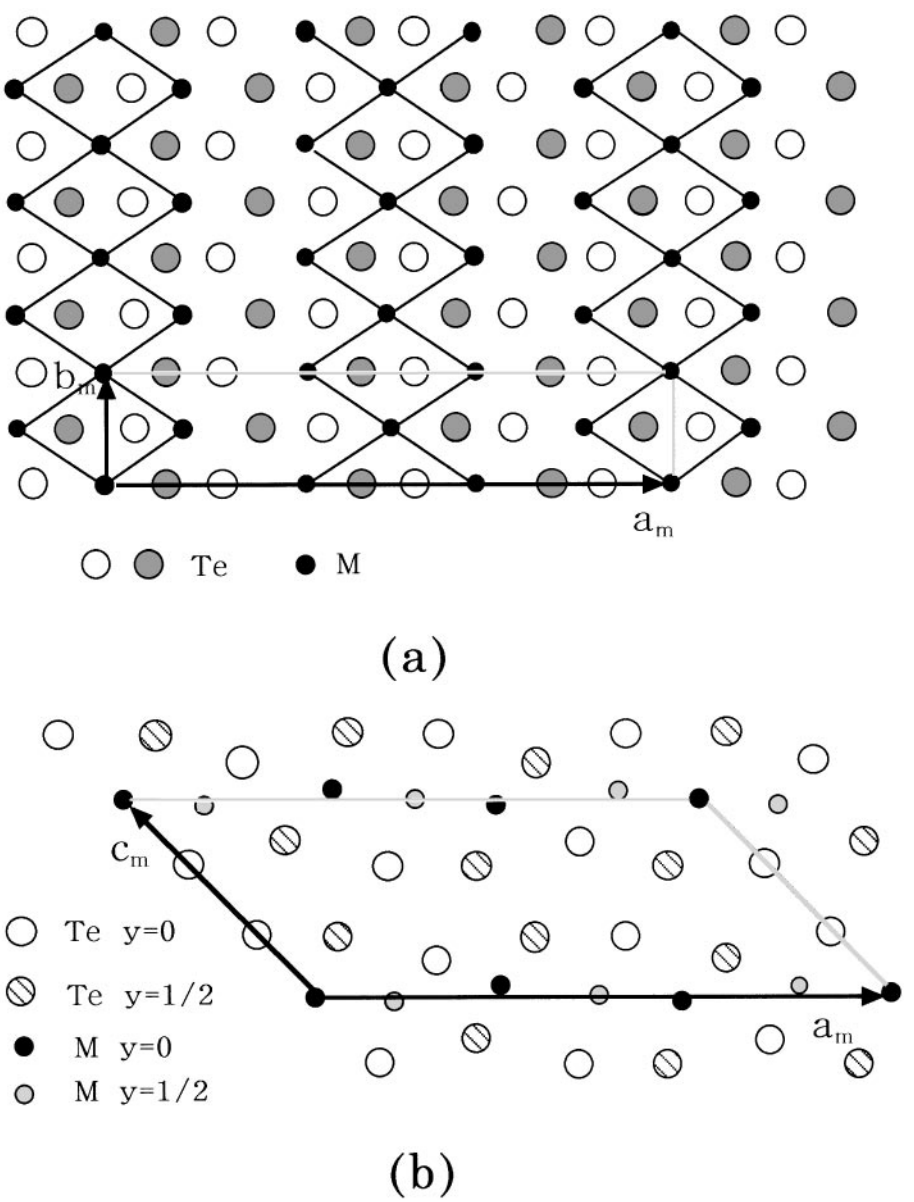

FIG. 1. Crystal structure of $1T$-$M\mathrm{Te}_2$. (a) Projection view of a Te–M–Te sandwich layer onto the (001) plane in a direction perpendicular to layers. Small and closed circles are M atoms. Open circles and dark gray circles are, respectively, Te atoms above and below the metal atom sheet. Two-thirds of M atoms shift from undistorted octahedral sites. The shortened M–M distances in double zigzag chains are drawn by solid lines. (b) Projection view of two Te–M–Te sandwich layers along the b axis. a_m, b_m, and c_m are the unit cell parameters of a monoclinic superlattice. Cell dimensions are $a_m = 19.39$ Å, $b_m = 3.642$ Å, $c_m = 9.375$ Å, and $\beta = 134°35'$ for $NbTe_2$ and $a_m = 19.31$ Å, $b_m = 3.651$ Å, $c_m = 9.377$ Å, and $\beta = 134°13'$ for $TaTe_2$ (6).

B ($z = 0.2898$) and C ($z = 0.2148$), where z is the refined parameter for atomic positions along the c axis (6). However, Bengel *et al.* (17) suggest from partial density calculations that the lowest-lying Te atoms at the C site should appear brightest in the STM images, because these Te atoms induce the higher density of p_z-like states near the Fermi level. The double zigzag chains of metal atoms are not imaged explicitly. The dimension of a unit cell on the STM image in Fig. 2b is OP = 3.6 Å and PQ = 11 Å and an intersection angle is 60°, in almost agreement with the X-ray values. Here it is worth noting that the double zigzag chains of metal atoms are considered to be intermediate between the $\sqrt{13} \times \sqrt{13}$ clusters of d^1 configuration of $1T$-TaS_2 and the zigzag chains of d^2 configuration of $1T$-$MoTe_2$. It is well-known that $1T$-TaS_2 brings about a CDW distortion at various temperatures and that commensurate CDW's below 180 K form the hexagonal superlattice which has a $\sqrt{13} \times \sqrt{13}$ unit cell rotated by 13.9° from an atomic lattice

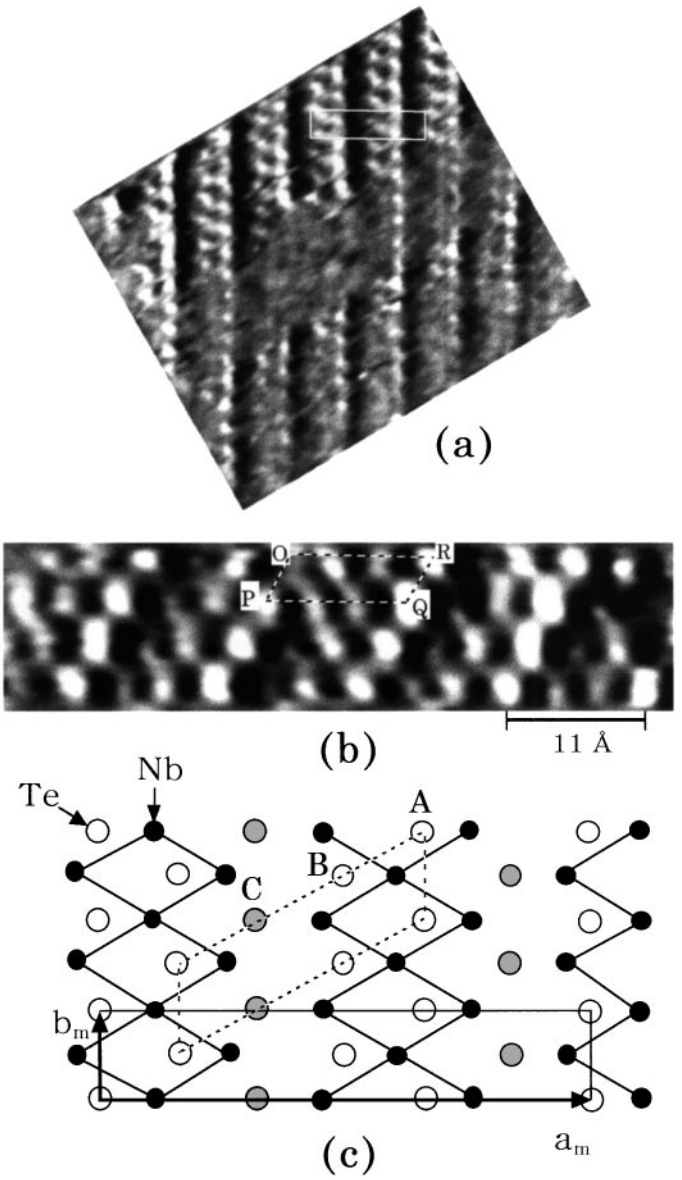

FIG. 2. STM images of $1T$-$NbTe_2$. (a) Large-scale STM image, which shows double or triple rows of bright spots stretching along the b axis. A rectangle which is shown by white lines is the unit cell of a monoclinic superlattice. (b) Small-scale STM image, which shows three different kinds of Te sites. (c) Relationship between the STM images and the crystal structure at the surface. Te atoms at the site A is extremely protruded outside a surface.

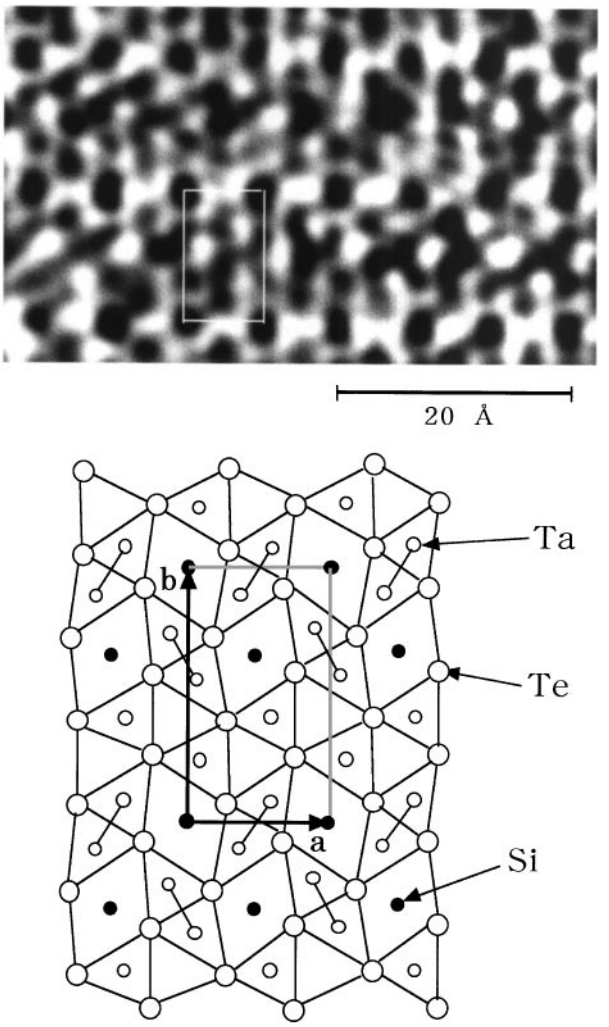

FIG. 3. STM image and crystal structure of Ta_3SiTe_6. A two-dimensional unit cell in the (a, b) plane is shown by a rectangle. The lattice constants are given by $a = 6.32$ Å and $b = 11.41$ Å.

(18–21). Our STM image for $1T$-TaS_2 at room temperature shows a superlattice due to quasi-commensurate CDWs and the outward appearances are similar to those of Thomson *et al.* (17) measured at 295 K. The periodicity and the rotation angle are 11.8 Å and 14°, respectively, which are in close agreement with those of the commensurate superlattice.

Figure 3 shows the crystal structure and the STM image of Ta_3SiTe_6. It contains two different types of Ta and Te atoms in a crystal, that is, paired and isolated atoms (9, 10). Metal atoms are located near the center of a trigonal prism with six Te atoms at the corners. It appears that the STM images are more or less affected by a tip-force induced surface corrugation as has been indicated by Bengel *et al.* (11). They have also indicated from a comparison with calculated density plots that isolated Te atoms are imaged more brightly than paired Te atoms. However, it is not confirmed by the present STM study. Our image shows dark spots at four corners of a rectangle which are assigned to Si sites. Both paired and isolated Te atoms are imaged as bright spots. The different behavior on the STM images would be caused by the difference in the magnitudes of the tip-force induced surface corrugation which is more likely to occur in ambient measurements as in the Bengel *et al.* work, because the tip-surface distance is shorter in ambient than in

UHV. In practice, their theoretically expected STM pattern indicates that all surface Te atoms are imaged almost equally in the absence of the tip-force induced corrugation (11).

XPS and ISEELS Results of $1T$-MTe_2

Before we discuss the XPS and ISEELS results of $1T$-$TaTe_2$ and $1T$-$NbTe_2$, a brief description is given on the Ta $4f$ XPS and Ta $N_{6,7}$ ISEELS spectra in $1T$-TaS_2. Their spectra are shown in Fig. 4. Our Ta $4f$ XPS spectrum at room temperature is similar to that of Hughes and Pollak (22). Each s.o. component consists of an asymmetrical broad peak and a large tail on the higher energy side, which result from the CDW distortion and the Mahan–Nozieres–de Dominicis (MND) effect, the many body effect which arises from the electron-hole pair creation around E_F (23, 24). Then the relative intensity of the $4f_{7/2}$ to the $4f_{5/2}$ line is deviated largely from the statistical value of 4/3. At lower temperature the main peak for each s.o. component splits into two peaks due to CDWs. Its splitting is about 0.69 eV at 14 K (22), although a higher-energy-resolution ultraviolet photoelectron spectroscopy (UPS) spectrum gives the energy splitting of 0.73 eV at 120 K (25). Similarly, the Ta $N_{6,7}$ ISEELS spectrum at room temperature reveals a broad peak for each s.o. component and an extended peak on the higher-energy side. The latter peak arises from the single-electron excitation of Ta $4f$ electrons to upper conduction bands and the MND effect. Figure 4a shows a large peak below the threshold. This is a bulk plasmon peak, the higher-energy tail of which affects the line intensities.

Figure 5 shows the Ta $4f$ XPS and Ta $N_{6,7}$ ISEELS spectra in $1T$-$TaTe_2$. The XPS spectrum shows only a dominant peak for each s.o. component. The further splitting and the broadening of the peak cannot be observed although the peak shifts by 0.6 eV to lower energy and a small structure appears at 25.8 eV. (The XPS spectrum is shifted by 1.1 eV to higher energy to compare with the ISEELS spectra. Then the small peak is found at 26.9 eV in Fig. 5). Here it is noted that the Ta $4f$ lines become sharper and the higher-energy tail diminishes although the shift of metal atoms is much larger than that of $1T$-TaS_2 ($\sim$0.1 Å). Similar changes of spectra have been observed by Eppinga *et al.* (24) for the Sn intercalation compounds of 2H-TaS_2. The Ta $4f$ lines after intercalation become sharper and the higher-energy tail diminishes. In the latter case the MND effect and the asymmetric broadening of the Ta $4f$ lines are supressed by filling the narrow d_{z^2} band with electrons transferred from Sn atoms, because electron-hole pair creation within the d_{z^2} band declines as the electron number increases upon intercalation. The occupancy of the d_{z^2} band of the trigonal-prism-coordination type of LTMDs such as

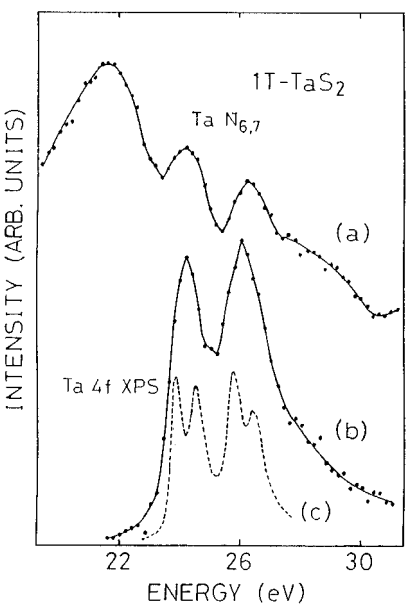

FIG. 4. Ta $4f$ XPS spectrum and Ta $N_{6,7}$ ISEELS spectrum in $1T$-TaS_2. (a) Ta $N_{6,7}$ ISEELS spectrum at the incident energy of 100 eV and the modulation voltage of 1 V. The threshold energy is about 23 eV. A large peak on the lower energy side is a bulk plasmon. (b) Ta $4f$ XPS spectrum at room temperature, which is shift by 1.2 eV to higher energy to aline the s.o.-split peaks. (c) Ta $4f$ XPS spectrum measured by Hughes and Pollak at 14 K (20), which is shifted by 0.8 eV to higher energy.

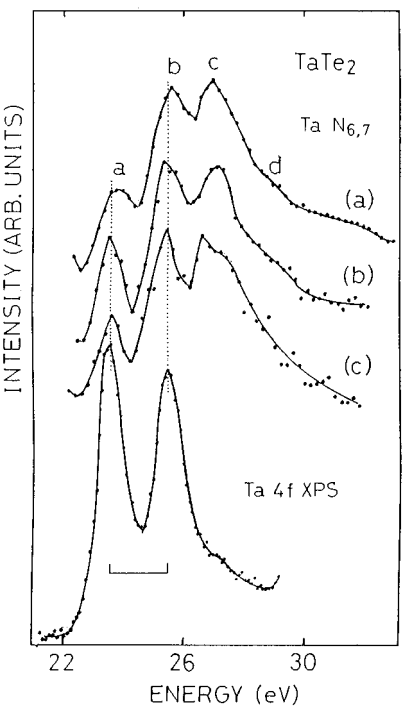

FIG. 5. Ta $N_{6,7}$ ISEELS spectra in $1T$-$TaTe_2$ at the incident energies of (a) 130 eV, (b) 100 eV, and (c) 70 eV and Ta $4f$ XPS spectrum. The XPS spectrum is shift by 1.1 eV to higher energy to aline the s.o.-split peaks.

2H-TaS_2 is two per metal atom and half of the states are filled for the unintercalated material. Then the product of number of occupied and unoccupied d_{z^2} states decreases monotonously as charge transfer occurs from intercalate species to the d_{z^2} band. For the 1T type of LTMDs, however, the occupancy of the lowest unoccupied t_{2g} band is six per metal atom. Then the MND effect enlarges until the electron number exceeds three per metal atom. Since the formal d electron count is 4/3 for 1T-$TaTe_2$, we may expect a larger MND effect in contrast to the experimental result. If the crystal distortion brings about further splitting of t_{2g} levels due to the Yahn-Teller effect and changes the occupancy of the lowest d band into two per metal atom, similar discussion is valid. At present, however, there is no evidence for the occurrence of the energy gap within the t_{2g} band. The Ta $N_{4,5}$ ISEELS spectra in Figs. 5a–5c reveal a doublet for each s.o. component. The energies of the main features are tabulated in Table 1 together with the XPS values. It is found that an energy separation between peaks a and b almost agrees with that of the peaks c and d and the s.o. splitting of Ta 4f core levels (1.9 eV). Then the peaks a and c are assigned to the Ta N_7 components and the peaks b and d are attributed to the N_6 components.

A similar doublet is found in the Te $N_{4,5}$ ISEELS spectra. The spectrum at lower incident energy shows four peaks at 40.4, 42.1, 43.6, and 45.3 eV although the Te 4d XPS spectrum reveals only two peaks owing to the s.o.-splitting of the core levels (see Fig. 6). Similar results are obtained for $NbTe_2$. The Te $N_{4,5}$ ISEELS spectrum in Fig. 7 exhibits three peaks at 40.2, 42.0, and 45.0 eV and a small shoulder at 43.0 eV although the Te 4d XPS spectrum does two peaks which are tabulated in Table 2. The first and third structures (notations a and c in Figs. 6 and 7) are assigned to the N_5 components and the second and fourth structures (b and d) are attributed to the N_4 components, although the N_4–N_5 separation is larger by about 0.4 eV than the s.o.

TABLE 1
Energies in eV of Main Features of Ta 4*f* XPS and Ta $N_{6,7}$ ISEELS Spectra

	1T-TaS_2				2H-TaS_2	1T-$TaTe_2$		Ta_3SiTe_6
	XPS			ISSELS	XPS	XPS	ISSELS	XPS
	$T = 295$ K		$T = 121$ K					
Ta 4$f_{7/2}$	23.18[a]	23.0	23.12[b]	24.2	23.0[c]	22.4	23.5	21.7
(Ta N_7)	23.72		23.85				27.0	25.0
Ta 4$f_{5/2}$	25.11	24.8	25.05	26.2	24.8	24.3	25.5	23.5
(Ta N_6)	25.65		25.78				29.0	26.9

[a]Ref. (22).
[b]Ref. (25).
[c]Ref. (26).

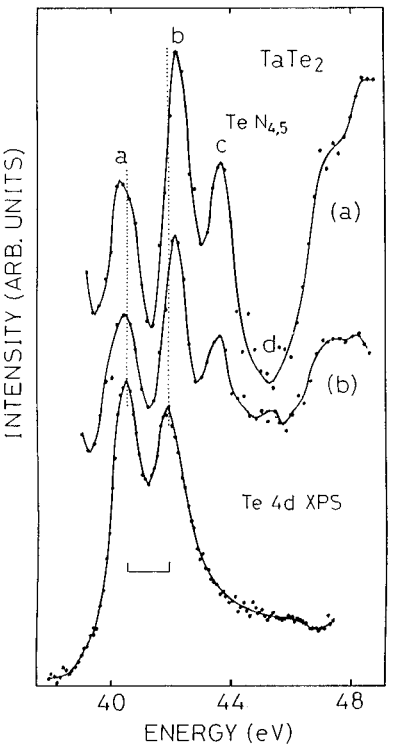

FIG. 6. Te $N_{4,5}$ ISEELS spectra in 1T-$TaTe_2$ at the incident energies of (a) 130 eV and (b) 100 eV and Te 4d XPS spectrum. The XPS spectrum is shift by 0.5 eV to higher energy to aline the s.o.-split peaks. The s.o. splitting is larger by 0.4 eV in ISEELS than in XPS.

splitting obtained from the XPS spectrum. Such a disagreement has already been found for Pb 5d levels in lead chalcogenides (27). For the Pb $O_{4,5}$ optical reflection spectra we have no doublets which are directly related to the s.o. splitting of the core levels. Recently, the present author has shown that four peaks observed in the Pb $O_{4,5}$ ISEELS spectra are related to the s.o.-split peaks, by measuring the spectra at large momentum transfer that optically forbidden transitions are allowed (28). He has confirmed the suggestion of Cardona *et al.* (27) that the disagreement is caused by the transfer-matrix element effect due to strong s.o. interaction present in the conduction electrons. Electron transitions in optical reflection and ISEELS at small momentum transfer obey dipole selection rules and an excited electron from a core level transfers to empty states just above the Fermi level. Then the spectra reflect the partial density of unoccupied states as well as the core levels while the ISEELS spectra at large momentum transfer come to represent the total density of unoccupied states, not so strongly depending on the band character. As in XPS an excited electron transfers to the continuum levels, the spectra are little affected by the band character and the density of unoccupied states. Moreover, an excited electron no longer participates in the screening of a core hole in XPS unlike in ISEELS and optical reflection. Finally, we suggest

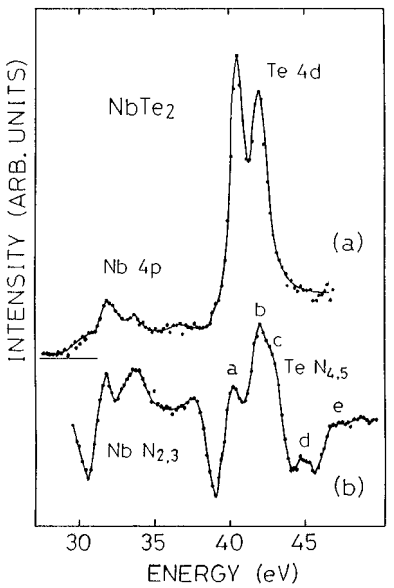

FIG. 7. Te 4d XPS and Te $N_{4,5}$ ISEELS spectra in $1T$-$NbTe_2$, which are, respectively, accompanied with Nb 4*p* and Nb $N_{2,3}$ structures on the lower energy side. Nb 4*d* XPS structures are affected by the Mg $K\alpha_{3,4}$ satellites of Te 4*d* lines which appear at 8.4 and 10.2 eV below a main peak.

that the apparent disagreement in the s.o. splittings is caused by different final states and transfer matrix elements in XPS and ISEELS.

In both the Ta $N_{6,7}$ and the Te $N_{4,5}$ ISEELS spectra the energy separations between the peaks *a* and *c* are coincided. A careful consideration shows that the peaks do not represent the density of unoccupied states near the Fermi level and that the doublets are caused by valence fluctuation in the final states as discussed later. The energy band calculations and the XAS spectra of the $1T$ type of LTMDs indicate that the t_{2g}–e_g splitting is 2.0–2.3 eV for TiS_2, 1.5 eV for ZrS_2 and 2.0 eV for HfS_2 (29, 30). For $1T$-MTe_2 there are no available band calculations which allow the estimation. It is ascertained in a previous paper (31) that the near-edge structures of the Nb $N_{2,3}$ ISEELS spectrum in NbS_2 and related compounds well represent the partial density of unoccupied states. Then the t_{2g}–e_g splitting has been estimated from a Nb $N_{2,3}$ spectrum in Fig. 7 to be about 1.9 eV. This value is comparable with the crystal-field splittings of undistorted $1T$-$TiTe_2$ and $ZrTe_2$ (29). As a result, the e_g structure in the Ta N_7 component would overlap the t_{2g} structure in the N_6 component, because the t_{2g}–e_g splitting is almost equal to the s.o. splitting. Similarly, the e_g structure in the Te N_5 component would appear in the neighborhood of the t_{2g} structure in the N_4 component. On the other hand, the Nb $N_{2,3}$ spectrum reveals no structures around 3 eV above the first peak in contrast with the Ta $N_{6,7}$ and Te $N_{4,5}$ spectra. Finally, it is concluded that the unidentified peaks of the Ta $N_{6,7}$ and Te $N_{4,5}$ ISEELS spectra, which are located at 3 eV above the main peak, can not be explained in terms of the energy band structure of unoccupied states.

TABLE 2
Energies in eV of Main Features of Te 4*d* XPS and Te $N_{4,5}$ ISEELS Spectra

	$1T$-$TaTe_2$		$1T$-$NbTe_2$		Nb_3SiTe_6	
	XPS	ISEELS	XPS	ISEELS	XPS	ISEELS
Te $4d_{5/2}$	40.0	40.4	39.6	40.2	40.0	40.8
(Te N_5)		43.6		43.0		44.2
		47.0		47.0		45.8?
Te $4d_{3/2}$	41.4	42.1	41.0	42.0	41.0	42.2
(Te N_4)		45.3		45.0		45.8?
		48.5		48.6		48.0

XPS and ISEELS Results of M_3SiTe_6

The Ta 4*f* XPS spectrum in Ta_3SiTe_6 reveals a doublet for each s.o component. As described above, Ta_3SiTe_6 contains two different kinds of Ta atoms in a crystal, that is, isolated and paired Ta atoms. The formal *d*-electron count is considered to be $5d^1$ for isolated Ta atoms and $5d^2$ for paired Ta atoms, so that the charge equilibrium condition requires the chemical formula of $(Ta^{3+})_2Ta^{4+}Si^{2+}(Te^{2-})_6$ (13). Oxygen adsorption strengthens the two valence states. Thus we assign the lower- and higher-energy peaks of a doublet to Ta^{3+} and Ta^{4+}, respectively. In Fig. 8 the XPS spectrum is compared with the Ta $N_{6,7}$ ISEELS spectrum in $1T$-$TaTe_2$. It is found that there is a good coincidence between the spectra in spite of the difference in crystal structure and electronic structure. The result implies that the four peaks in the Ta $N_{6,7}$ ISEELS spectrum arise from two different kinds of Ta atoms. Since the ground state is uniquely determined from the XPS spectrum in Fig. 5, they are originated from the two different final states of Ta^{3+}* $4f^{13}5d^2$ and Ta^{4+}* $4f^{13}5d^1$.

Figure 9 shows the Te 4*d* XPS structure and the Nb $N_{2,3}$ and Te $N_{4,5}$ ISEELS structures for Nb_3SiTe_6. The Te 4*d* XPS spectrum gives no clear evidences of different Te atoms which are confirmed by the STM and AFM images (11). It reveals only a peak for each s.o. component although the peak is somewhat broadened and the peak separation due to s.o. interaction decreases apparently. The Nb $N_{2,3}$ spectrum shows small peaks at 1.6 and 2.6 eV above the first peak. The near-edge structures are different from those of NbS_2 in spite of the same coordination of metal atoms (31). They are rather similar to those of $1T$-$NbTe_2$. The difference is caused by bonding interaction with Si atoms and stronger Nb–Nb and Nb–Te interaction. According to the energy band calculations of Nb_3GeTe_6 and Ta_3SiTe_6, which are akin to those of Nb_3SiTe_6, a small density of

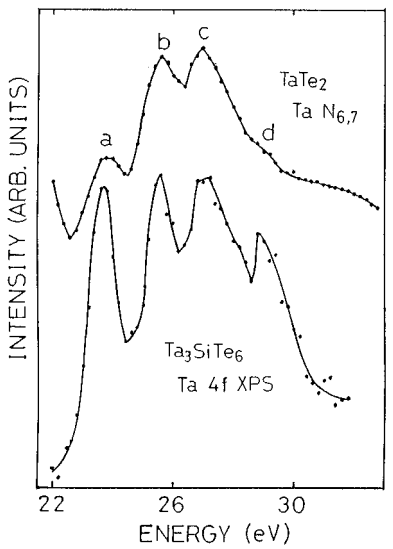

FIG. 8. Comparison between the Ta 4*f* XPS spectrum in oxygen-adsorbed Ta_3SiTe_6 and the Ta $N_{6,7}$ ISEELS spectra in 1*T*-$TaTe_2$. The XPS spectrum is shift by 1.8 eV to higher energy.

unoccupied states of a Nb 4d character exists at the Fermi level (9, 13). Then the compounds exhibit metallic properties. Of course, metal *d* orbitals are strongly hybridized with Te 5*p* orbitals. The next set of metal *d* bands are separated from the unoccupied states by an energy gap, the maximum density being located around 2.5 eV above the Fermi level. Unoccupied Ge 4*p* or Si 3*p* states exists on the higher energy side. The upper metal *sp* bands are not calculated for these compounds. However, the energy band structure of Nb_2GeTe_4, which is constructed of the same building units as Nb_3GeTe_6, shows that metal *sp* bands are in the range of 5 to 10 eV above the Fermi level (13). The Nb $N_{2,3}$ near-edge structures in Fig. 9 are consistent with the results of the band calculations except for unoccupied states below the energy gap. The first peak represents the maximum density of unoccupied Nb 4*d* states and a small peak at 2.6 eV represents unoccupied Si 3*p* states which are mixed with Nb 4*d* states. It is noted that the near-edge structures of the Te $N_{4,5}$ ISEELS spectrum are apparently dissimilar to both the energy band structure and the Nb $N_{2,3}$ structures. An unidentified peak appears at 3.5 eV above the main peak for each s.o. component and a whole appearance rather resembles that of MTe_2. Despite of the facts, a broad peak at 48 eV may be assigned to the N_4 component of the upper metal *sp* bands. The last assignment has been made from comparison with the Nb $M_{4,5}$ ISEELS spectrum and the energy band structure of Nb_2GeTe_4. The Nb $M_{4,5}$ ISEELS spectrum in Fig. 10 shows a small peak and a large peak at 2.7 and 5.4 eV above the first peak, respectively. Taking the s.o. splitting of Nb 3*d* core-levels into account, the small peak is assigned to the main peak in the M_4 component. The M_5/M_4 intensity ratio is found to be deviated largely from a statistical value and the M_5 component is dominant over the M_4 component. It is suggested from comparison with the Te $N_{4,5}$ spectrum that the large peak as well as the

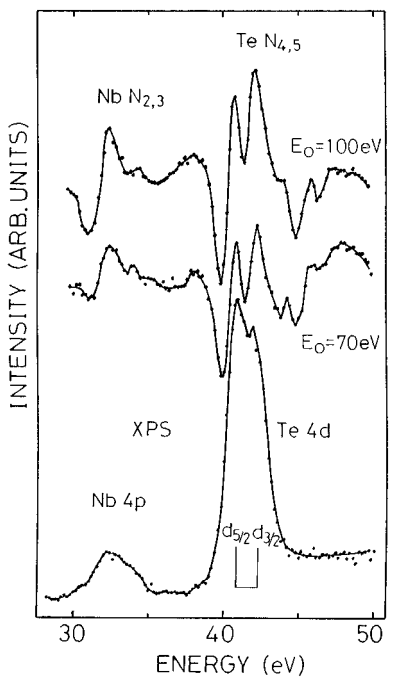

FIG. 9. Te 4*d* XPS and Te $N_{4,5}$ ISEELS spectra in Nb_3SiTe_6, which are, respectively, accompanied with Nb 4*p* and Nb $N_{2,3}$ structures on the lower energy side. Nb 4*d* XPS structures are affected by the Mg $K\alpha_{3,4}$ satellites of Te 4*d* lines.

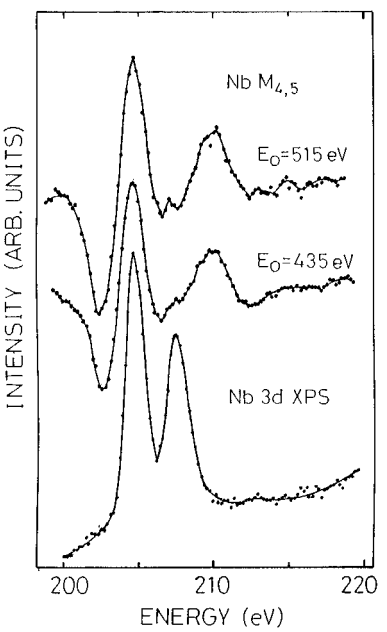

FIG. 10. Nb 3*d* XPS and Nb $M_{4,5}$ ISEELS spectra in Nb_3SiTe_6. The s.o. splitting of the core levels is esimated to be about 2.8 eV.

broad peak is assigned to the metal *sp* bands in the Nb M_5 and Te N_4 parts, respectively, because the energy distances from the main peaks are coincided within experimental errors (see Fig. 11). It is believed that the Te $N_{4,5}$ ISEELS spectrum represent the partial density of states as well as the other ligand XAS and ISEELS spectra of LTMDs. Apparent disagreements with the energy band structure are caused by the appearance of an unidentified peak at 2.8–3.5 eV above the main peak and the s.o. splitting of the core levels. Finally, if an unidentified peak appears in the Te N_4 component, it would be observed near the N_5 structure of the metal *sp* bands.

Final State Effects on the Ta 4f and Te 4d XPS and ISEELS Spectra

The Pb 5*d* and Te 4*d* XPS spectra in oxygen-adsorbed PbTe reveal a doublet for each s.o. component (27). In this case the doublet arises from two different valence states with or without bonding with oxygen. In other words, it arises from *two different kinds of initial states*. The chemical shift due to oxygen adsorption is about 4.0 eV for Te 4*d* levels. For the Ta $N_{6,7}$ and Te $N_{4,5}$ ISEELS spectra in 1*T*-MTe_2 a doublet arises from *two different kinds of final states*. At least the Ta 4*f* and Te 4*d* XPS spectra show only a peak for each s.o. component. As discussed above, the Te 5*p*-derived valence bands overlap metal *d* bands significantly and both metal *d* and Te 5*p* bands have unoccupied states near the Fermi level which can be filled with electrons transferred from a core level. This band overlap is enhanced by lattice distortion and the double zigzag chain structure favors electron transfer from Te to *M* atoms. The *d*-electron count is given by $d^{1+\varepsilon}$ ($0 < \varepsilon < 1$). The tight-binding calculation for distorted VTe_2 has predicted that 0.25 electrons per V atom is transferred from Te atoms (7). The *noninterger* *d* electron count is regarded as resonance between two valence states, that is, M^{3+} d^2 and M^{4+} $5d^1$. The XPS spectrum reveals a small peak at 25.8 eV as described above. This peak might be assigned to Ta^{4+} and the main peak at 22.4 eV is attributed to Ta^{3+}. However, the intensity relative to the main peak is smaller than expected from the *d*-electron count. Thus we may suggest that the screening of a core hole plays an important role on the Ta 4*f* XPS spectrum in $TaTe_2$ as well as in 1*T*-TaS_2 and the main peak should be assigned to the well-screened final state of Ta^{3+*} $4f^{13}5d^2$.

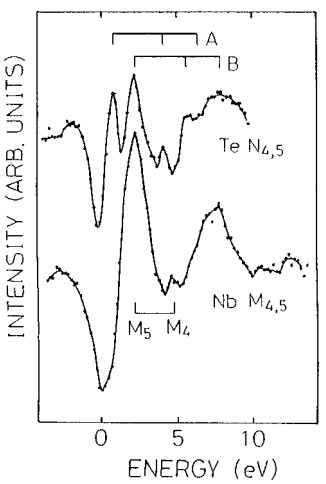

FIG. 11. Comparison between the Te $N_{4,5}$ and Nb $M_{4,5}$ ISEELS spectra in Nb_3SiTe_6.

Figures 12a and 12b show a schematic diagram for Ta $N_{6,7}$ transitions to explain the Ta $N_{6,7}$ ISEELS spectrum in 1*T*-$TaTe_2$. The near-edge structures arise from electron transitions from Ta 4*f* core-levels to unoccupied states near the Fermi level. For simplicity we assume that a Ta atom prior to excitation is in the ground state of Ta^{4+} which possesses a 5*d* electron. If a 4*f* electron transfers to an unoccupied state in the Ta 5*d*-derived conduction bands, leaving a hole in the core level, the electron configuration of the final state is given by $4f^{13}5d^2$ (Fig. 12a). In the intraatomic transitions a transferred electron contributes to the screening of the core hole. If a 4*f* electron transfers to an unoccupied state in the Te 5*p*-derived valence bands, the final state is given by $4f^{13}5d^1$ and the core hole is poorly screened (Fig. 12b). The final state $|4f^{13}5d^2\varepsilon^n\rangle$ may be lowered in energy with respect to the final state $|4f^{13}5d^1\varepsilon^{n+1}\rangle$ by electron relaxation in an excited atom, where ε^n is all valence and conduction electrons excluding valence electrons in an excited atom. Then the ISEELS spectra show two peaks corresponding to the final states of Ta^{3+*} $4f^{13}5d^2$ and Ta^{4+*} $4f^{13}5d^1$. The poorly screened core hole in Ta^{4+*} might provoke spontaneous electron-transfer from adjacent Te atoms. This process is regarded as the shake-up process, although it requires no extra transfer energy because the Fermi level intersects both metal *d* and Te 5*p* bands. The final state is identical to that of the $4f \rightarrow 5d$ intraatomic transitions. Therefore, both transitions cannot be distinguished. The same processes are considered for Ta^{3+} in the ground state. However, it is considered that the probability of creating the final state of Ta^{2+*} $4f^{13}5d^3$ is too small to observe a peak because the excitation energy is much larger than that of the final state $|4f^{13}5d^2\varepsilon^n\rangle$ due to strong repulsive *d*–*d* interaction. If the core hole of Ta^{3+*} is well screened, a transferred electron from a core level would travel throughout a crystal and no additional electron transfer occur from neighboring Ta or Te atoms. Finally, the ISEELS spectra show two peaks corresponding to the final states of Ta^{3+*} $4f^{13}5d^2$ and Ta^{4+*} $4f^{13}5d^1$. For 1*T*-TaS_2 the S 3*p*-derived valence bands are filled with electrons completely. In that case the threshold structures arise from only the intraatomic Ta 4*f* to 5*d* transitions and the resulting core hole is well-screened by an excited electron. Then the ISEELS spectrum shows a prominent peak corresponding to Ta^{3+*} $4f^{13}5d^2$ for each s.o. component.

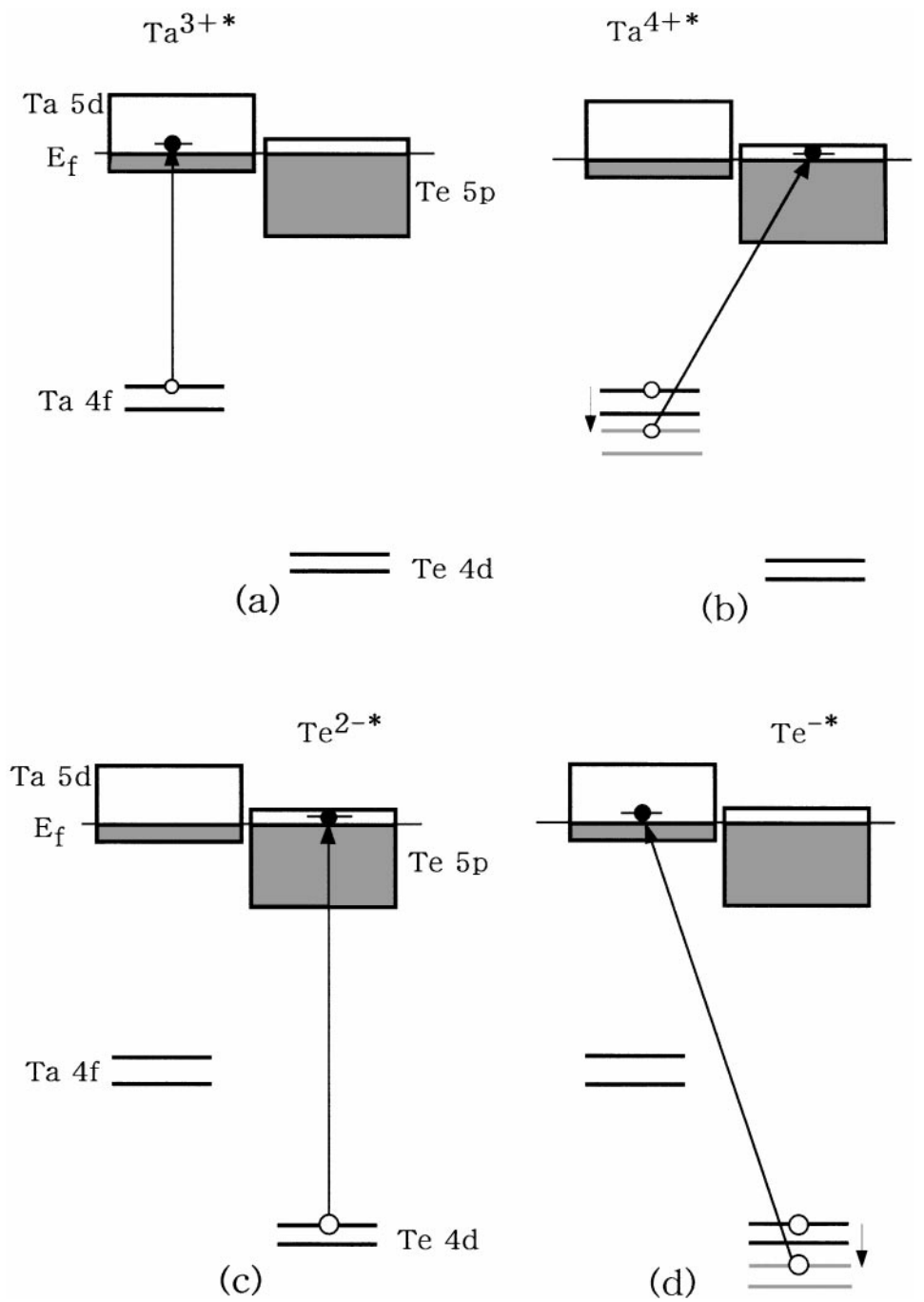

FIG. 12. Schematic diagram for valence fluctuation in the final states of Ta $N_{6,7}$ and Te $N_{4,5}$ transitions. For $1T$-$TaTe_2$ the Fermi level intersects the Ta 5*d* and Te 5*p* bands which overlap each other, so that both bands contain unoccupied states just above the Fermi level. (a) As a 4*f* electron in Ta^{4+} transfers to an unoccupied Ta 5*d* state, for example, the final state is given by $Ta^{3+*}\ 4f^{13}5d^2 + \varepsilon^n$, where ε^n is all valence and conduction electrons excluding electrons in an excited atom. (b) As the 4*f* electron transfers to an unoccupied Te 5*p* state, then the final state is given by $Ta^{4+*}\ 4f^{13}5d^1 + \varepsilon^{n+1}$. (c) As a 4*d* electron in Te^- transfers to an unoccupied Te 5*p* state, for example, the final state is given by $Te^{2-*}\ 4d^9 5d^6 + \varepsilon^n$. (d) As the 4*d* electron transfers to an unoccupied Ta 5*d* state, then the final state is given by $Te^{-*}\ 4d^9 5d^5 + \varepsilon^{n+1}$. Thus the core-electron tansitions of Ta^{4+} and Te^- give rise to two different kinds of final states, that is, the well-screened final state and the poorly screened final state. The core levels in the poorly screened final states are pulled down by stronger Coulomb attractive force of a nucleus.

Figures 12c and 12d show a schematic diagram for Te $N_{4,5}$ transitions to explain the Te $N_{4,5}$ ISEELS spectra in $1T$-$M\mathrm{Te}_2$. For simplicity we assume that a Te atom prior to excitation is in the ground state of Te^- which has five $5p$ electrons. If a Te $4d$ electron is excited to an unoccupied state in the Te $5p$ bands, leaving a hole in the core level, the electron configuration of the final state is given by Te^{2-*} $4d^95p^6$ (Fig. 12c). In the intraatomic transitions a transferred electron contributes to the screening of a core hole as well as other valence electrons. On the other hand, if a Te $4d$ electron transfers to an unoccupied state in the metal d bands, the Te atom after excitation has the final state of Te^{-*} $4d^95p^5$ (Fig. 12d). If the core hole is screened with other valence electrons insufficiently, the Coulomb attractive force might provoke spontaneous electron-transfer from adjacent *Te* atoms or metal stoms. As the electron transfer occurs, the final state is Te^{2-*} $4d^95p^6$ which is identical to that of the intraatomic transitions. For Te^{2-} no Te $4d \rightarrow 5p$ intraatomic transitions occur because the $5p$ levels are filled completely with electrons. Then Te^{2-} has the sole final state of Te^{2-*} $4d^95p^6$. Finally, the Te $N_{4,5}$ ISEELS spectra show two peaks corresponding to the final states of Te^{2-*} $4d^95p^6$ and Te^{-*} $4d^95p^5$. It is considered that a well-screened Te^{2-*} peak appears at lower energy than a poorly screened Te^{-*} peak. For $M_3A\mathrm{Te}_6$ the top of the valence bands are unoccupied as well. Then it is expected that the Te $N_{4,5}$ ISEELS spectra show near-edge structures similar to those in $1T$-$M\mathrm{Te}_2$, which is consistent with the experimental result.

CONCLUSIONS

The STM images of $1T$-$M\mathrm{Te}_2$ show double or triple rows of bright spots which are directed to the b axis. The Te $4d$ XPS spectra give no clear evidence of three different Te sites which are confirmed by the STM images. Similarly the Ta $4f$ XPS spectrum makes no distinction among Ta atoms in double zigzag chains. It reveals a dominant peak for each s.o. component. It is found from comparison with the XPS spectra of $1T$-TaS_2 that the Ta $4f$ lines are sharper in spite of the larger shift of metal atoms from ideal octahedral sites and the higher-energy tail which results from the MND effect diminishes. The result is contradictory to a simple consideration based on the electron occupancy of the lowest t_{2g} conduction band of the undistorted $1T$ type of LMTD. The Ta $N_{6,7}$ and Te $N_{4,5}$ ISEELS spectra, on the other hand, reveal a doublet for each s.o. component. We have suggested that the doublet arises from the unique band structure of these telluride compounds for which Te $5p$ bands overlap metal d bands significantly and two different kinds of unoccupied states exist near the Fermi level. Electron transitions from the core levels to the unoccupied states give rise to two different kinds of final states, i.e., Ta^{3+*} and Ta^{4+*} for Ta $N_{6,7}$ transitions and Te^{-*} and Te^{2-*} for Te $N_{4,5}$ transitions. This phenomenon is regarded as valence fluctuation in the final states.

For NbTe_2 the t_{2g}–e_g splitting is estimated from the Nb $N_{2,3}$ ISEELS spectrum to be about 1.9 eV. For $\mathrm{Nb_3SiTe_6}$ it is found that Si $3p$ unoccupied states are located around 2.6 eV above the maximum density of Nb $4p$ states and that the metal sp bands extend in the range of 5 to 10 eV above the Fermi level. The experimental results are almost in agreement with the band calculations.

REFERENCES

1. J. A. Wilson and Y. D. Yoffe, *Adv. Phys.* **18,** 193 (1969).
2. "Physics and Chemistry of Materials with Layered Structures" (E. Mooser, Ed.), Vols. 1–5 Reidel, Boston, 1976–1979.
3. "Surface Properties of Layered Structures" (G. Benedek, Ed.). Kluwer Academic. Boston, 1992.
4. "Incommensurate Sandwiched Layered Compounds" (A. Meerschaut, Ed.), Trans Tech. Switzerland, 1991.
5. Y. Ohno, *J. Solid State Chem.* **134,** 99 (1997).
6. B. E. Brown, *Acta Cryst.* **20,** 264 (1966).
7. E. Canadell, S. Jobic, R. Brec, J. Rouxel, and M. H. Whangbo, *J. Solid State Chem.* **99,** 189 (1992).
8. M. H. Whangbo and E. Canadell, *J. Am. Chem. Soc.* **114,** 9587 (1992).
9. M. Evain, L. Monconduit, A. van der Lee, R. Brec, J. Rouxel, and E. Canadell, *New J. Chem.* **18,** 215 (1994).
10. J. Li, M. E. Badding, and F. J. DiSalvo, *J. Alloys Comp.* **184,** 257 (1992).
11. H. Bengel, H. J. Cantow, M. Evain, S. N. Nagonov, and M. H. Whangbo, *Surf. Sci.* **365,** 461 (1996).
12. W. Liang, M. H. Whangbo, M. Evain, L. Monconduit, R. Brec, H. Behgel, H. J. Cantow, and S. N. Magonov, *Chem. Matter* **6,** 678 (1994).
13. F. Boucher, V. Zhukov, and M. Evain, *Inorg. Chem.* **35,** 7649 (1996).
14. Y. Ohno, *Phys. Rev. B* **36,** 7500 (1987).
15. S. J. Kim, S. J. Park, H. J. Oh, I. C. Jeon, and S. Song, *Bull. Korean Chem. Soc.* **15,** 1098 (1994); and S. J. Kim, S. J. Park, I. C. Jeon, C. Kim, C. Pyun, and K. A. Yee, *J. Phys. Chem. Solids* **58,** 659 (1997).
16. H. Bengel, H. J. Cantow, S. N. Magonov, and M. H. Whangbo, *Adv. Mater.* **7,** 483 (1995).
17. H. Bengel, H. J. Cantow, S. N. Magonov, D. Jung, J. Ren, and M. H. Whangbo, *New. J. Chem.* **20,** 287 (1996).
18. J. A. Wilson, F. J. DiSalvo, and S. Mahajan, *Adv. Phys.* **24,** 117 (1975).
19. M. H. Whangbo, J. Ren, E. Canadell, D. Louder, B. A. Parkinson, H. Bengel, and S. N. Magonov, *J. Am. Chem. Soc.* **115,** 3760 (1993).
20. R. V. Coleman, Z. Dai, W. W. Mcnairy, C. G. Slough, and C. Wang, *in* "Scanning Tunneling Microscopy" (J. A. Stroscio and W. J. Kaiser, Eds.), p. 349. Academic Press, New York, 1993.
21. R. E. Thomson, B. Burk, A. Zettl, and J. Clarke, *Phys. Rev. B* **49,** 16899 (1994).
22. H. P. Hughes and R. A. Pollak, *Phil. Mag.* **34,** 1025 (1976).
23. G. D. Mahan, *Phys. Rev.* **163,** 612 (1967).
24. C. Nozieres and C. T. de Dominicis, *Phys. Rev.* **178,** 1097 (1969).
25. R. A. Pollak, D. E. Eastman, F. J. Himpsel, P. Heimann, and B. Reihl, *Phys. Rev. B* **24,** 7435 (1981).
26. R. Eppinga, G. A. Sawatzky, C. Haas, and C. F. van Bruggen, *J. Phys. C* **9,** 337 (1976).
27. M. Cardona, C. M. Penchina, E. E. Koch, and P. Y. Yu, *Phys. Status Solidii B* **53,** 327 (1972).
28. Y. Ohno, *Phys. Rev. B* **49,** 7851 (1994).
29. D. W. Bullet, *J. Phys. C* **11,** 4501 (1978).
30. Y. Ohno, K. Hirama, S. Nakai, C. Sugiura, and S. Okada, *Phys. Rev. B* **27,** 3811 (1983).
31. Y. Ohno, *Phys. Rev. B* **48,** 5515 (1993).